11. J. Schnadt et al., Nature 418, 620 (2002).
12. N. A. Anderson and T. Lian, Annu. Rev. Phys. Chem. 56, 491 (2005).
13. R. Huber, S. Spörlein, J. E. Moser, M. Grätzel, J. Wachtveitl, J. Phys. Chem. B 104, 8995 (2000).
14. A. Fujishima, K. Honda, Nature 238, 37 (1972).
15. M. R. Hoffmann, S. T. Martin, W. Choi, D. W. Bahnemann, Chem. Rev. 95, 69 (1995).
16. A. Hagfeldt, M. Grätzel, Acc. Chem. Res. 33, 269 (2000).
17. R. Wang et al., Nature 388, 431 (1997).
18. A. L. Linsebigler, G. Lu, J. T. Yates Jr., Chem. Rev. 95, 735 (1995).
19. S. H. Szczepankiewicz, A. J. Colussi, M. R. Hoffmann, J. Phys. Chem. B 104, 9842 (2000).
20. K. Onda, B. Li, H. Petek, Phys. Rev. B 70, 045415 (2004).
21. U. Diebold, Surf. Sci. Rep. 48, 53 (2003).
22. M. A. Henderson, Surf. Sci. 355, 151 (1996).
23. I. M. Brookes, C. A. Muryn, G. Thornton, Phys. Rev. Lett. 87, 266103 (2001).
24. R. Schaub et al., Phys. Rev. Lett. 87, 266104 (2001).
25. H. Petek, S. Ogawa, Prog. Surf. Sci. 56, 239 (1997).
26. M. A. Henderson, W. S. Epling, C. H. F. Peden, C. L. Perkins, J. Phys. Chem. B 107, 534 (2003).
27. J. Leconte, A. Markovits, M. K. Skalli, C. Minot, A. Belmajdoub, Surf. Sci. 497, 194 (2002).
28. M. A. Henderson, Surf. Sci. Rep. 46, 1 (2002).
29. To confirm that both H₂O molecules and OH are essential, we hydroxylated the stoichiometric surface, which does not exhibit the resonance when exposed to H₂O, with H atoms from a thermal cracking source (36). As anticipated, the dissociation of H₂O at bridging O vacancies and the reduction of bridging O atoms by gas phase H atoms (40) provide two alternative protocols for the detection of the wet-electron state.
30. The calculations with the Vienna ab Initio Simulation Package code use the generalized gradient approximation with the spin-polarized Perdew-Wang exchange-correlation functional. The oxygen 1s and Ti 1s to 3p are treated as core states. We use the projector augmented-wave (PAW) potential, which is generally more accurate than the ultrasoft pseudopotential. The surface is modeled by periodically repeated slabs containing three Ti layers separated by 10 Å vacuum gaps. A Monhkorst-Pack grid of (3×3×1) k points is used for the (1×2) surface unit cell. Molecules are adsorbed on both sides of the slab to avoid formation of a dipole moment. The positions of all atoms are allowed to relax until the force acting on each is less than 0.02 eV Å⁻¹. We use a 400-eV plane-wave cutoff for the optimization and a 520-eV cutoff for the static calculation of the electronic structure.
31. G. Kresse, J. Hafner, Phys. Rev. B 47, 558 (1993).
32. G. Kresse, J. Hafner, Phys. Rev. B 48, 13115 (1993).
33. G. Kresse, J. Hafner, Phys. Rev. B 49, 14251 (1994).
34. J. P. Perdew, Y. Wang, Phys. Rev. B 45, 13244 (1992).
35. G. Kresse, J. Joubert, Phys. Rev. B 59, 1758 (1999).
36. S. Suzuki, K. Fukui, H. Onishi, Y. Iwasawa, Phys. Rev. Lett. 84, 2156 (2000).
37. C. Gahl, U. Bovensiepen, C. Frischkorn, M. Wolf, Phys. Rev. Lett. 89, 107402 (2002).
38. C. Gahl et al., Surf. Sci. 532-535, 108 (2003).
39. M. Chander, Y. Z. Li, J. C. Patrin, J. H. Weaver, Phys. Rev. B 48, 2493 (1993).
40. B. Li et al., data not shown.

Deterministic Coupling of Single Quantum Dots to Single Nanocavity Modes

Antonio Badolato,[1]* Kevin Hennessy,[1]* Mete Atatüre,[3] Jan Dreiser,[3] Evelyn Hu,[1,2] Pierre M. Petroff,[1,2] Atac Imamoğlu[3]†

We demonstrate a deterministic approach to the implementation of solid-state cavity quantum electrodynamics (QED) systems based on a precise spatial and spectral overlap between a single self-assembled quantum dot and a photonic crystal membrane nanocavity. By fine-tuning nanocavity modes with a high quality factor into resonance with any given quantum dot exciton, we observed clear signatures of cavity QED (such as the Purcell effect) in all fabricated structures. This approach removes the major hindrances that had limited the application of solid-state cavity QED and enables the realization of experiments previously proposed in the context of quantum information processing.

Cavity QED experiments, where single atoms are strongly coupled to single cavity modes, have culminated in the demonstration of conditional quantum dynamics (1), quantum nondemolition measurement of photons, and creation of entanglement between three distinguishable quantum systems (2). The realization of such systems in the solid state, although challenging, offers several advantages (3). Indeed, a monolithically integrated cavity QED system consisting of a self-assembled quantum dot (QD) embedded within a nanocavity could have vanishing uncertainty in the relative location of the emitter with respect to the cavity electric field maxima and could allow for much stronger emitter-cavity coupling because of the ultrasmall cavity volumes. A number of experiments have already demonstrated the potential of QD-based solid-state cavity QED in applications such as single-photon sources (4–6). Nonetheless, because it is very difficult to predetermine the exact resonance energy and location of an optically active QD, all of the prior QD-based cavity QED experiments relied on a random spectral and spatial overlap between QDs and cavity modes (7–9). The difficulty in tuning the resonance energy of a fabricated nanocavity and the reduced likelihood of spatial overlap for the ultrasmall cavities of interest have so far limited the application of these solid-state cavity QED nanostructures. We demonstrate a deterministic approach to the QD nanocavity coupling based on two crucial components: (i) a positioning technique that allows us to locate a single QD at an electric field maximum of a photonic crystal (PC) nanocavity with 25-nm accuracy, and (ii) a precise spectral tuning of the cavity mode into resonance with any given QD emission line. This deterministic QD cavity coupling yields a spontaneous emission rate enhancement (Purcell effect) of the QD luminescence in all four fabricated devices.

Our basic material was a semiconductor heterostructure (Fig. 1A) grown by molecular beam epitaxy (10). The emitter-cavity system comprised free-standing PC membranes fabricated in a 180-nm layer of GaAs (10) with coherently embedded QDs. The square-lattice PC pattern with a single missing hole (S1) fabricated in the GaAs membrane can support a nondegenerate donor-type mode with a high quality factor (Q) and an ultrasmall mode volume (11).

The first key ingredient of our approach was the active positioning of a QD within the PC defect that eliminated the uncertainty in the relative position of the QD with respect to the cavity mode. We grew six vertically correlated InAs/GaAs QD layers (12, 13) in the GaAs membrane (Fig. 1A, right). The emission energy of the first QD layer (seed QD) was blue-shifted by in situ annealing the QDs when partly capped with GaAs (14). Five successive as-grown QD layers (stacked QDs) were stacked up to the surface (15), forming a tracer for the seed QD that was detectable by scanning electron microscopy (SEM). By resolving the location of a QD on the surface, we were able to determine the location of the seed QD that was of interest for coupling to a nanocavity. A matrix of gold markers was fabricated on the low-density QD region ($\approx 2 \times 10^5$ cm^{-2}) to map the isolated QDs relative to this matrix. With the use of electron beam lithography, we wrote the S1-PC pattern offset by the appropriate distance from the markers (16). The small white dot in Fig. 1B shows the SEM trace of the surface QD in one of our four devices (device I), which was positioned within 25 nm from one of the four

[1]Department of Electrical and Computer Engineering, [2]Materials Department, University of California, Santa Barbara, CA 93106, USA. [3]Institute of Quantum Electronics, ETH-Hönggerberg, CH-8093 Zürich, Switzerland.

*These authors contributed equally to this work.
†To whom correspondence should be addressed. E-mail: imamoglu@phys.ethz.ch

calculated electric field maxima of the S1-PC defect region (Fig. 1C) (17).

Before cavity fabrication, we measured the emission spectrum of each targeted seed-stack QD with the use of cryogenic temperature microphotoluminescence (μ-PL) (10). This spectrum allowed us to verify that our targeted QDs were truly stacked, as we observed the emission from the excited states of the stacked QDs along with the blue-shifted exciton emission from the seed QD. Likewise, by identifying the exciton lines according to the power dependence of the μ-PL emission intensities, we verified that no unstacked seed QDs had nucleated in close proximity and selected only seed-stack QDs with unambiguous spectra. We then designed our nanocavities (11) to ensure that the high-Q cavity mode resonance (M) was near the seed QD exciton energies but remained red-shifted relative to those energies. In this way, we were able to fabricate devices that had cavity resonances with Q values up to 5000 and red-shifted by 13 ± 3 nm with respect to the QD exciton lines. The comparison of the QD-cavity spectrum with the QD spectrum before cavity fabrication allowed us to identify the different modes of the S1-PC. Because test cavities located in regions with no QDs did not show any cavity mode emission, we conclude that in our devices with one seed-stack QD the cavity modes were primarily sustained by excited states of the stacked QDs.

The second key ingredient of our work was the tuning of M through the μ-PL spectrum of the targeted seed QD after PC fabrication. We developed a digital etching (18) technique that fine-tuned M by controllably enlarging PC holes and thinning the PC membrane. One etching cycle consisted of selectively removing the native surface oxide of our devices in a solution of citric acid (1 M) and allowing the material to grow a new native oxide layer under atmospheric conditions. Because the entire process is self-limiting, the etched layer thickness per cycle was essentially the same, resulting in a digital (i.e., stepped) etching process (10). As shown in Fig. 2A, we obtained blue-shift of M at ~3 nm per cycle without detriment to the Q factor. We emphasize that because of this stepped tuning, we were able to follow the blue-shift of M cycle by cycle—without affecting the QD—and to stop our process as soon as we engaged the QD. With this high tuning accuracy, we could count on blue-shifting (or red-shifting) the QD exciton energy by applying a magnetic field (19) (or by increasing the temperature) to reach the exact QD-cavity resonance.

By applying three digital etching cycles to device I, we were able to blue-shift M within 6.6 nm of the charged exciton (X$^-$) line (red curve in Fig. 2B). Because the linewidth of M is only 0.3 nm ($Q \approx 3000$), it is safe to assume there is no M-X$^-$ coupling for such a de-

tuning, and thus we refer to this stage as off-resonance. After etching for two additional cycles, we observed (at 4.2 K) a reduction of the M-X$^-$ detuning to 0.6 nm together with an enhancement of the X$^-$ intensity by a factor of 11, and an even larger increase in the M line (blue curve in Fig. 2B) (20). This striking change in the QD spectrum is direct evidence of a nontrivial cavity QED effect; namely, the QD-cavity coupling is strong enough that even for a finite detuning exceeding the corresponding linewidths, the QD emission intensity and the multi-exciton dynamics are drastically modified.

As we raised the temperature of device I, the X$^-$ line red-shifted more than the M line, thereby achieving resonance at 39 K (Fig. 3A). The bottom curve in Fig. 3A shows that even at a low pump power [0.38 P_{sat}, where P_{sat} (0.59 μW) is defined as the pump power needed to saturate the neutral exciton (X)], the spectrum is dominated by the X$^-$ line on-resonance with an intensity enhancement factor of 43 with respect to the X$^-$ line off-resonance. As shown in Fig. 3B, no M line was detected in the off-resonance case for $P \leq 0.38 P_{sat}$. As mentioned above, the cavity

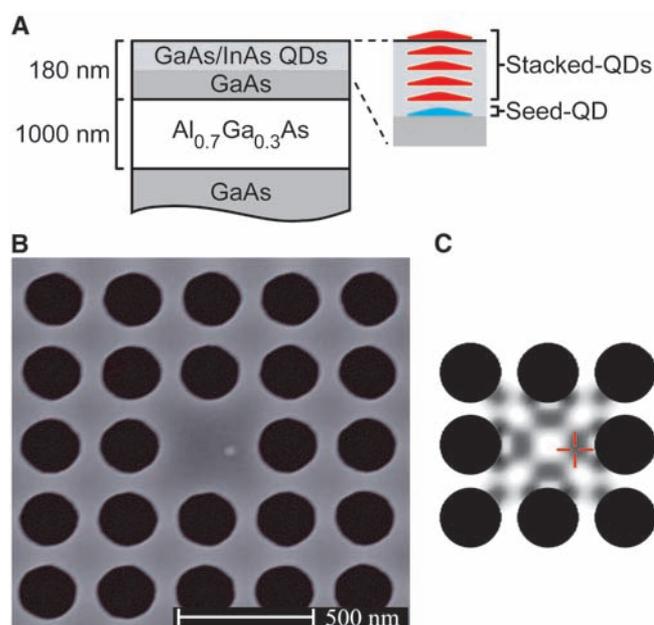**Fig. 1.** (**A**) Schematic cross section of the semiconductor heterostructure. (**B**) SEM image of the S1-PC defect region in device I. The small white dot is the top QD of the targeted seed stack. (**C**) Plot of the electric field intensity present in the semiconductor of the S1-PC defect region, calculated by three-dimensional finite-difference time domain (25). Cavity-mode maxima correspond to darker gray levels. The red cross indicates the position of the seed stack.
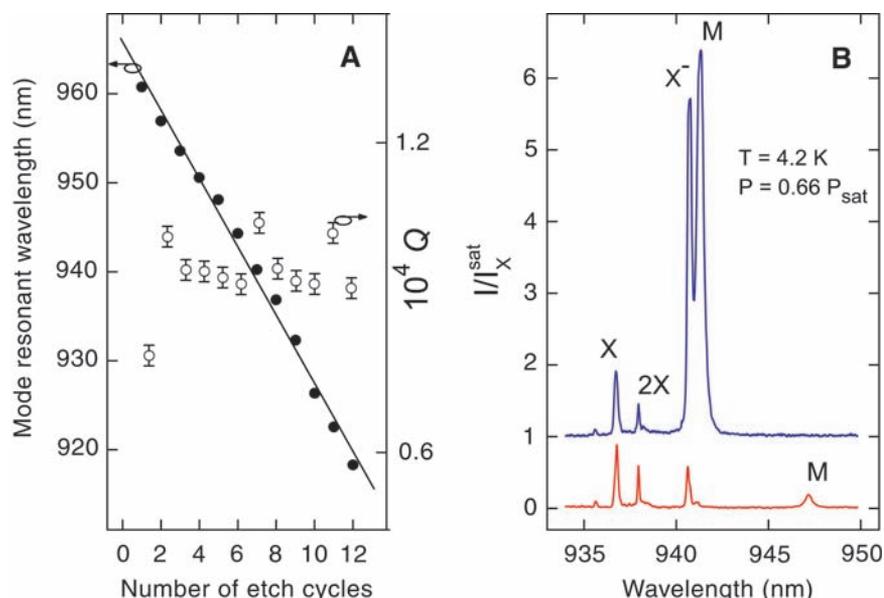

Fig. 2. (**A**) Resonant wavelength of the high-Q mode and Q versus the number of etching cycles for S1-PCs fabricated in the high-density QD region and measured at 4.2 K. The solid line is a guide for the eye. (**B**) Device I μ-PL spectra (10) at 4.2 K and pump power of 0.66 P_{sat}. Red curve, spectrum after three digital etching cycles; blue curve (offset for clarity), spectrum after five digital etching cycles. The y axis is normalized to I_X^{sat}, the neutral exciton (X) μ-PL intensity at saturation (20).
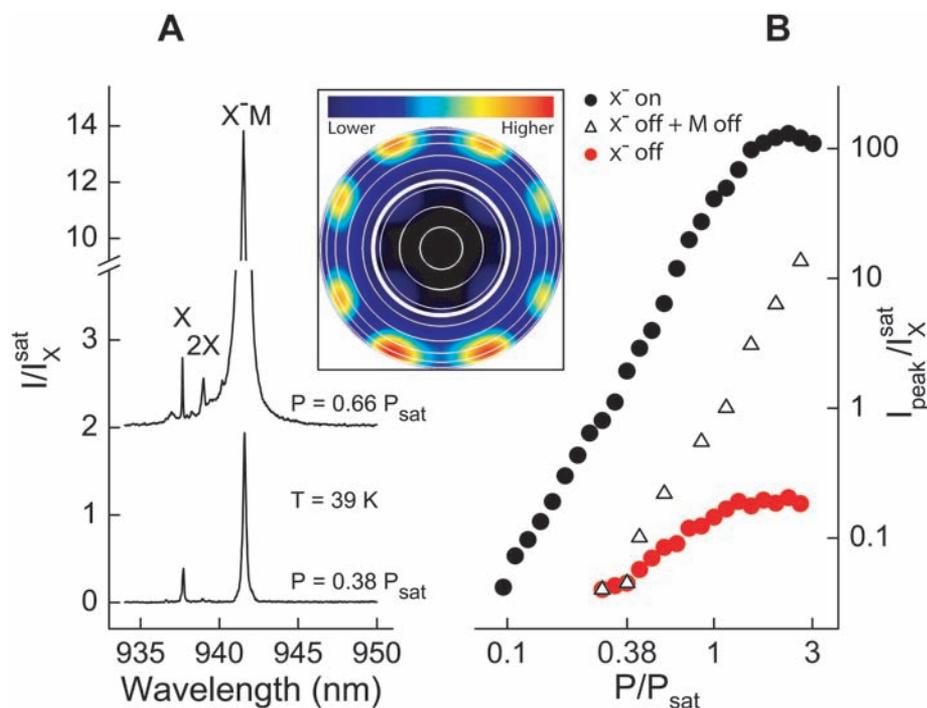
Fig. 3. Device I. (**A**) μ-PL spectra after five digital etching cycles measured at 39 K. The X⁻ is on-resonance with the cavity mode (X⁻M) (*20*). The two curves correspond to different excitation powers: 0.38 P_{sat} (bottom curve) and 0.66 P_{sat} (upper curve, offset for clarity). Inset: Far-field profile of a classical dipole emitting into the PC mode, calculated over a hemisphere of radius 1 m by a fully vectorial algorithm from the near-field dipole fields (*26*). Plotted is $\mathbf{E} \times \mathbf{H}$ normal to the hemisphere surface, where the emission angle is shown in 10° increments with white circles. The thicker white circle corresponds to the numerical aperture (0.55) of our objective. (**B**) Peak maximum intensities versus pump power (log-log scale) of X⁻ off-resonance (solid red dots), sum of X⁻ and M both off-resonance (open triangles), and X⁻ on-resonance (solid black dots). The x axis is normalized to the X saturation pump power and the y axis to the X saturation intensity (*20*).
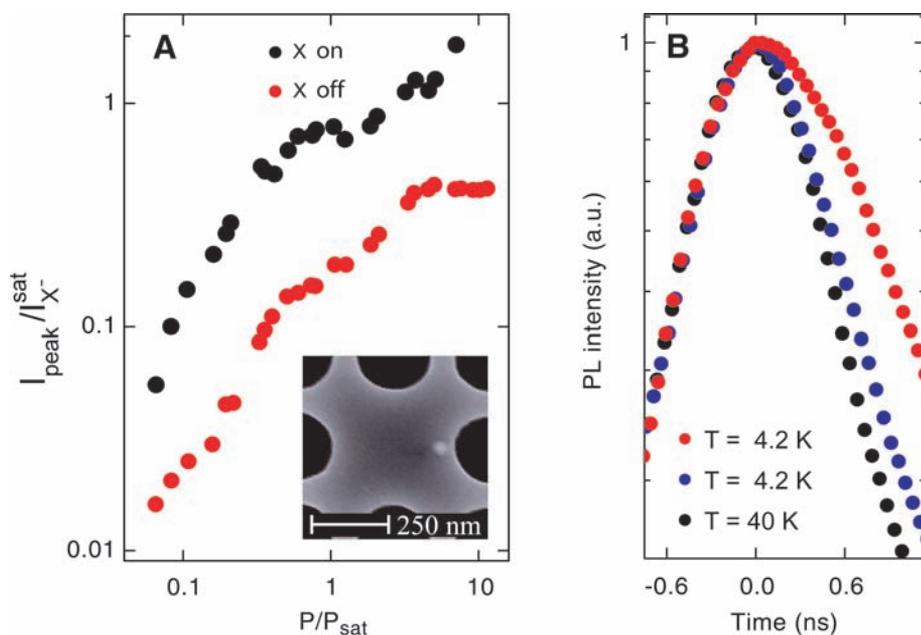

Fig. 4. Device II. (**A**) Peak maximum intensity versus pump power (log-log scale) of X off-resonance (solid red dots) and X on-resonance (solid black dots). Because the X⁻ at saturation remained independent of the M-X detuning, the x axis is normalized to the X⁻ saturation pump power and the y axis to the X⁻ saturation intensity. (Inset) SEM image of the S1-PC defect region. The small white dot is the top QD of the targeted seed stack. (**B**) Lifetime, as measured by TCSPC, of the X line off-resonance at 4.2 K (solid red dots), near-resonance at 4.2 K (solid blue dots), and on-resonance at 40 K (solid black dots).

modes off-resonance are sustained by the excited states of the stacked QDs, and we consider this background contribution to the X⁻M peak intensity as a constant factor independent of the QD-cavity detuning. Therefore, the actual resonant cavity enhancement of QD emission can be obtained by subtracting this constant factor from the total peak intensity. The remarkable enhancement of X⁻ peak intensity, ranging from a factor of ~20 at $P = 0.29\ P_{sat}$ to a factor of ~700 at $P = 2.3\ P_{sat}$, directly proves the resonant coupling between the seed QD and the PC cavity. We note that in contrast to other solid-state cavities, the S1-PC tends to diffract the far-field radiation (Fig. 3, inset) away from the collection cone of an objective having the optical axis orthogonal to the PC membrane. Consequently, we argue that the large increase of the X⁻ peak intensity above saturation indicates a substantial Purcell enhancement of the QD radiative decay rate. In device I, time-correlated single photon counting (TCSPC) measurements (*10*) showed resolution-limited lifetimes (<0.7 ns) of X⁻ both near- and on-resonance. Hence, we were not able to infer the reduction in emission time by directly measuring the decay time.

In device II, after first tuning the M and X lines with the use of digital etching and then temperature tuning (40 K), we observed at low pump powers only a factor of 5 enhancement of the X intensity from off- to on-resonance (Fig. 4A). This weaker coupling was predicted, as the position of the surface QD in the SEM image (Fig. 4A, inset) showed a reduced spatial overlap with the simulated electric field maxima of the S1-PC defect region (*21*, *22*). In this case, we were able to observe directly the effect of QD-cavity spectral resonance on the X lifetime (τ), which continually decreased from off- to near-resonance, reaching the resolution limit of our TCSPC setup at the exact resonance (Fig. 4B). By deconvolving the TCSPC response function, we extracted a lifetime on-resonance (τ_{on}) of 0.2 ± 0.1 ns (at 40 K), near-resonance of 0.6 ns (at 4.2 K), and off-resonance (τ_{off}) of 1 ns (at 4.2 K). These results not only directly prove that we can achieve enhancement of radiative decay rate by a factor of ~5 even in devices with less precise positioning, but also corroborate our calculation-based claims that the enhancement of the exciton μ-PL intensity in the S1-PC is predominantly due to the Purcell effect.

Careful examination of the seed-QD multi-exciton dynamics shows that the physics unveiled by our experiments goes beyond the well-known Purcell effect. In device I (Figs. 2B and 3A), by comparing the bi-exciton (2X) μ-PL intensity at the same pump power (0.66 P_{sat}) for M-X⁻ off-, near-, and on-resonance, we observed a clear decrease of the 2X intensity (relative to the X intensity) as X⁻ reached the resonance. This reduction may be

explained in terms of sequential carrier capture by the QD: If electron capture in our QDs is more likely than hole capture, the creation of the 2X state requires that a QD in state X$^-$ capture an additional hole. Yet if the X$^-$ emission rate increases because of a large Purcell effect, the 2X emission will be reduced because the QD is less likely to capture the second hole before the X$^-$ recombines. On the basis of this observation, we conclude that a systematic study of the QD-cavity system, only feasible within a deterministic approach, can give new insights into the carrier capture and multi-exciton dynamics of the QDs.

The QD-cavity coupling coefficient (g) that we extract for our device I, using the data for the off- and near-resonance cases (Fig. 2B) and assuming a cavity enhancement of the collection efficiency by a factor of 20 (23), is $g \approx 80$ µeV. This value is only half the theoretical maximum for our cavity structure. The value of g as well as its insensitivity to positioning can be improved by using other PC-cavity designs that also exhibit higher Q values and higher fabrication defect tolerance.

By achieving a deterministic spatial and spectral overlap between a QD exciton line and a PC nanocavity mode, we have demonstrated the realization of a truly tunable solid-state cavity QED system and established a framework for the realization of a new set of cavity QED experiments previously implemented only in atomic systems. The broad implication of this research, however, can have some immediate application in several appealing directions, such as cavity-assisted QD spin-flip Raman transition for generation of indistinguishable single photons (24), coupling of two QDs to a single common cavity mode (25), and simultaneous coupling of a cavity mode to both X and 2X lines of a single QD.

References and Notes
1. Q. A. Turchette, C. J. Hood, W. Lange, H. Mabuchi, H. J. Kimble, *Phys. Rev. Lett.* **75**, 4710 (1995).
2. J. M. Raimond, M. Brune, S. Haroche, *Rev. Mod. Phys.* **73**, 565 (2001).
3. J. M. Gérard, in *Single Quantum Dots: Fundamentals, Application and New Concepts*, P. Michler, Ed., vol. 90 of *Springer Series in Topics in Applied Physics* (Springer, Berlin, 2003), pp. 269–314.
4. P. Michler et al., *Science* **290**, 2282 (2000).
5. E. Moreau et al., *Appl. Phys. Lett.* **79**, 2865 (2001).
6. C. Santori, D. Fattal, J. Vuckovic, G. S. Solomon, Y. Yamamoto, *Nature* **419**, 594 (2002).
7. J. P. Reithmaier et al., *Nature* **432**, 197 (2004).
8. T. Yoshie et al., *Nature* **432**, 200 (2004).
9. E. Peter et al., in preparation (available at http://xxx.lanl.gov/abs/quant-ph/0411076).
10. Fabrication and characterization details are available as supporting material on *Science* Online.
11. K. Hennessy et al., *Appl. Phys. Lett.* **83**, 3650 (2003).
12. Q. H. Xie, A. Madhukar, P. Chen, N. P. Kobayashi, *Phys. Rev. Lett.* **75**, 2542 (1995).
13. D. M. Bruls et al., *Appl. Phys. Lett.* **82**, 3758 (2003).
14. P. M. Petroff, A. Lorke, A. Imamoglu, *Phys. Today* **54**, 46 (2001).
15. The seed QD layer was grown 64 nm below the top surface of the membrane; successive stacked QD layers were spaced by 12 nm of GaAs.
16. K. Hennessy, A. Badolato, P. M. Petroff, E. Hu, *Photonics Nanostruct. Fund. Appl.* **2**, 65 (2004).
17. In the broad field of QD nanosystems, our positioning technique can provide enough accuracy to implement functional devices such as QDs coupled to nanoelectromechanical systems and electrical addressing of single QDs.
18. G. C. DeSalvo et al., *J. Electrochem. Soc.* **143**, 3652 (1996).
19. C. Schulhauser et al., *Phys. Rev. B* **66**, 193303 (2002).
20. Because the X µ-PL intensity at saturation (I_X^{sat}) remained independent of the M-X$^-$ detuning, we compare spectra at different tuning stages by normalizing them to I_X^{sat}. In this way, we rule out potential variations in optical alignment and laser power.
21. The distance between the QD on the surface and the closest hole surface was ~50 nm, which was large enough to keep the seed QD from interacting with the surface states as described in (22).
22. C. F. Wang et al., *Appl. Phys. Lett.* **85**, 3423 (2004).
23. This value is derived from a comparison of the on- and off-resonance µ-PL peak intensity for the lowest measured pump power 0.29 P_{sat} (Fig. 3B).
24. A. Kiraz, M. Atature, A. Imamoglu, *Phys. Rev. A* **69**, 032305 (2004).
25. A. Imamoglu et al., *Phys. Rev. Lett.* **83**, 4204 (1999).
26. These simulations were done with commercially available software from Lumerical Solutions.
27. Supported by NSF Nanoscale Interdisciplinary Research Team grant 0304678 (A.B. and P.M.P.), Binational Science Foundation grant 2000233 (A.B. and P.M.P.), NSF Integrative Graduate Education and Research Traineeship grant 9987618 (K.H. and E.H.), and internal grants from ETH Zürich (M.A., J.D., and A.I.). We thank Lumerical Solutions for detailed assistance with the far-field calculations.

The Highland Mangabey *Lophocebus kipunji*: A New Species of African Monkey

Trevor Jones,[1]* Carolyn L. Ehardt,[2] Thomas M. Butynski,[3] Tim R. B. Davenport,[4] Noah E. Mpunga,[4] Sophy J. Machaga,[4] Daniela W. De Luca[4]

A distinct species of mangabey was independently found at two sites 370 kilometers apart in southern Tanzania (Mount Rungwe and Livingstone in the Southern Highlands and Ndundulu in the Udzungwa Mountains). This new species is described here and given the name "highland mangabey" *Lophocebus kipunji* sp. nov. We place this monkey in *Lophocebus*, because it possesses noncontrasting black eyelids and is arboreal. *L. kipunji* is distinguished from other mangabeys by the color of its pelage; long, upright crest; off-white tail and ventrum; and loud call. This find has implications for primate evolution, African biogeography, and forest conservation.

The most recently discovered species of monkey in Africa was the sun-tailed monkey, *Cercopithecus solatus*, found in Gabon in 1984 (1). Here, we report on the discovery of a new species of mangabey in Tanzania. This discovery was made almost simultaneously by independent field-workers on different mountain ranges in southern Tanzania. We relate the circumstances of discovery in the two sites, describe and name the new species, and discuss its conservation status.

Southern Highlands population. The Southern Highlands of southwest Tanzania (Fig. 1) rise to 2961 m above sea level (asl) and comprise mountain ranges capped by forest-grassland mosaic. The Highlands receive rainfall via convectional uplift from Lake Nyasa of up to 2900 mm a year, the highest in Tanzania.

Within the Southern Highlands, the Tanzanian government is presently gazetting the Kitulo Plateau and adjacent Livingstone Forest as the Kitulo National Park (412 km^2, 09°00′S to 09°16′S and 33°43′E to 34°03′E) (2). Mount Rungwe Forest Reserve (150 km^2, 09°03′S to 09°12′ S and 33°35′E to 33°45′E) supports montane and upper montane forest, bamboo, and plateau grassland. The montane forests of Mount Rungwe and Livingstone (Rungwe-Livingstone) are joined only by a narrow corridor of degraded forest. Until now, eight species of primate were known from the Southern Highlands, including a probable new species of dwarf galago, *Galagoides* sp. (3).

During interviews in January 2003 in villages around Mount Rungwe, we heard rumors about a shy and atypical monkey known as *Kipunji* (kip-oon-jee). The local Wanyakyusa have a strong oral tradition based on both real and mythical forest animals, and validation of these rumors was protracted. We first observed an unusual primate during biodiversity surveys on Mount Rungwe in May 2003, but

[1]Udzungwa Mountains National Park, Box 99, Mang'ula, Tanzania. [2]Department of Anthropology, University of Georgia, Athens, GA 30602–1619, USA. [3]Conservation International, Post Office Box 68200, City Square 00200, Nairobi, Kenya. [4]Wildlife Conservation Society, Southern Highlands Conservation Programme, Post Office Box 1475, Mbeya, Tanzania.

*To whom correspondence should be addressed. E-mail: tembomkubwa@gmail.com